Liquid Cooled Aluminum Silicon Carbide Heat Sinks for

Reliable Power Electronics Packages

Darshan G. Pahinkar^{1*}, Lauren Boteler², Dimeji Ibitayo², Sreekant Narumanchi³, Paul Paret³, Douglas DeVoto³, Joshua Major³, Samuel Graham¹

¹Electronics Manufacturing and Reliability Laboratory, GWW School of Mechanical Engineering, Georgia Institute of Technology, Atlanta, GA 30332

²U. S. Army Research Laboratory, Adelphi, MD 20783

³National Renewable Energy Laboratory, Golden, CO 80401

* Corresponding author <u>-darshan@gatech.edu</u>

771 Ferst Drive NW, Atlanta, GA 30332

ABSTRACT

With recent advances in the state-of-the-art of power electronic devices, packaging has become one of the critical factors limiting the performance and durability of power electronics. To this end, this study investigates the feasibility of a novel integrated package assembly, which consists of copper circuit layer on an aluminum nitride (AIN) dielectric layer that is bonded to an aluminum silicon carbide (AISiC) substrate. The entire assembly possesses a low coefficient of thermal expansion (CTE) mismatch which aids in the thermal cycling reliability of the structure. The new assembly can serve as a replacement for the conventionally used direct bonded copper (DBC) – Cu base plate – Al heat sink assembly. While improvements in thermal cycling stability of more than a factor of 18 has been demonstrated, the use of AlSiC can result in increased thermal resistance when compared to thick copper heat spreaders. To address this issue, we demonstrate that the integration of single phase liquid cooling in the AlSiC layer can result in improved thermal performance, matching that of copper heat spreading layers. This is aided by the use of heat transfer enhancement features built into the AlSiC layer.

It is found that, for a given pumping power and through analytical optimization of geometries, either microchannels, pin fins and jets can be designed to yield a heat transfer coefficients of up to 65000 W m⁻² K⁻¹, which can result in competitive device temperatures as Cu-baseplate designs, but with added reliability.

Keywords - power electronics, thermal management, direct bonded copper, channels, single phase cooling, jet impingement, computational fluid dynamics (CFD).

1. INTRODUCTION

Power electronic components are widely used in applications from high voltage electric grid power management to low voltage battery chargers and encompass a broad power spectrum [1-3]. These devices help to control the current and voltage waveforms as power is transmitted between power sources and loads. A typical power electronic package contains an electronic device fabricated from silicon (Si) or a wide band gap material like silicon carbide (SiC) or gallium nitride (GaN) [4]. The devices are soldered on to a metallized dielectric substrate, which provides pathways to form the electric circuit, heat spreading, and electrical isolation from the other devices on the substrate. For high performance systems, substrates containing copper (Cu) metallization on aluminum nitride (AlN) dielectrics (e.g., direct-bonded copper or DBC) are used for mounting the power device circuitry. The substrate in turn is attached to a metal baseplate and a heat sink using a thermal interface material as shown in Fig. 1(a). Under thermal cycling, DBC substrates and solder layers are often subjected to complex state of stress due to mismatch between coefficients of thermal expansion (CTE) of different layers. As a result, delamination and cracking of DBC substrates are common [5, 6]. In addition to the potential failure of the DBC, the resistances imposed by multiple interfaces and layers used in the conventional DBC-cold plate packaging architecture, limit the ability to produce compact designs with low thermal resistance.

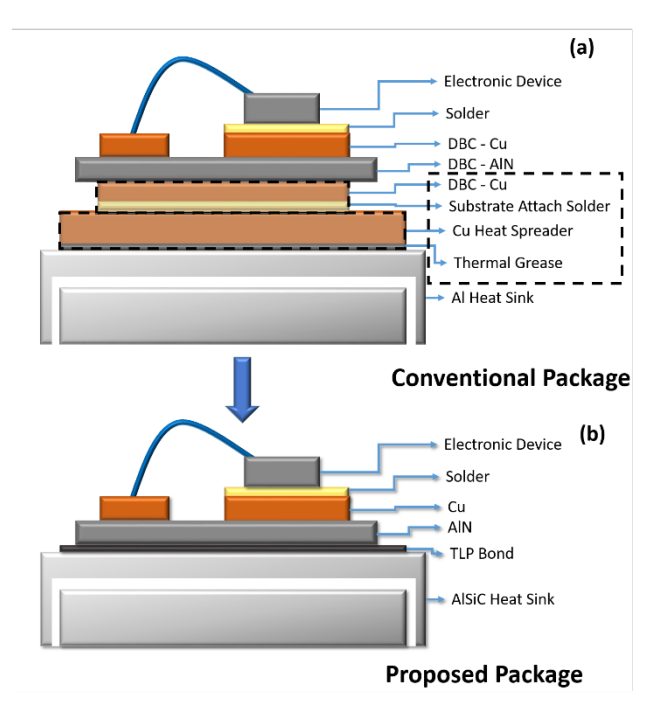


Figure 1. (a) Conventional power electronic package showing multiple material layers and interfaces. (b) Improved design considered in the present work showing Cu – AlN – TLP bond – AlSiC stacking. Cooling features are embedded in the AlSiC heat sink.

The issues raised in the reliability and design of the conventional packaging architecture utilizing DBC substrates and cold plates (Fig. 1(a)) are addressed in the package design undertaken in the present work. In this new design, an AlN dielectric substrate is directly bonded to an AlSiC baseplate/heat sink that has a similar CTE, as shown in Fig. 1(b) using a transient liquid phase (TLP) bonding approach [7]. The minimization of the CTE mismatch between the two layers results in a lower probability of fatigue and aging failures. Table 1 [8-10] shows the CTE and thermal conductivity of typical materials used in power electronic packaging.

Table 1. Thermal conductivity and CTE of materials used in electronics packaging at room temperature.

room temperature.		
Material	Coefficient of thermal	Thermal
	expansion (CTE)	Conductivity
	$(10^{-6} {\rm ^{o}C^{-1}})$	$(W m^{-1} K^{-1})$
Copper	16.5	395
Aluminum	22.2	200
Aluminum Nitride (AlN)	4.5	175
Silicon	4.0	148
Silicon Carbide (SiC)	4.0	280
Aluminum Silicon Carbide (AlSiC)	8.0	185
Copper Molybdenum (CuMo)	7.0	200
Copper Tungsten (CuW)	6.5	175

The details of this TLP bonding process as well as the thermal, mechanical and metallographic characterization of the bond material are reported elsewhere [7]. The thermal conductivity of the bond material was found to be $120 \pm 6 \text{ W m}^{-1} \text{ K}^{-1}$ (more than twice that of the typical solder materials), whereas its Young's modulus and hardness values were 84 GPa and 6.3 GPa, respectively (Young's modulus for AuSn solder is 59 GPa) [11]. Sixteen samples bonded with this technique, when subjected to thermal cycling between – 40°C to 150°C for 1800 cycles and aging tests at 150°C for 1400 hours, have shown no change in void fractions, no failures, cracking or delamination. Thus, along with favorable thermal, mechanical and fatigue strength properties exhibited by these bonds, the package thickness is reduced by up to 6 mm, compared to the conventional designs as shown in Fig. 1(b). Here, the structure under consideration has Cu – AlN – AlSiC heat sink, instead of DBC – solder – base plate – thermal grease – heat sink as in the conventional stack. It should be noted that the Cu layers in the DBC assist in heat spreading in the package, which is attributed to the high thermal conductivity of Cu layers. Therefore, as the amount of Cu in the stack is reduced or eliminated, the AlSiC heat sink bears the responsibility of effective heat spreading. Hence, cooling features must be introduced into the AlSiC heat sink to assist with the heat removal. These cooling features, namely mini- or microchannels, pin fins and impingement jets aid in heat transfer area

enhancement. Optimization of these features is essential for the package being developed in the present work, so that these features can compensate for the removal of Cu layers and make the device temperatures with the use of the improved package design competitive with the DBC-based packages.

The present work focuses on single-phase cooling to reduce the thermal resistance of the AlSiC baseplate packaging systems and to show that they can be competitive with DBC copper heat spreader designs. Single phase liquid cooling provides a better heat transfer coefficient than air-cooling under the same fluid flow conditions, and it has been extensively studied for novelty of designs. Zhou, Dede and Joshi [12] performed a computational analysis of a hybrid slot jet system, which combines a channel design and a slot jet geometry. They were able to achieve a heat transfer coefficient (HTC) of 34 kW m⁻² K⁻¹ at the heat sink with a pressure drop less than 10 kPa. In a similar fashion, Lau, Han, Yue, Lu and Xiaowu [13] fabricated a silicon microcooler, the design of which is a combination of spray cooling and microchannel cooling. Sakanova and Yin [14] conducted a computational investigation of cooling using microchannel structures embedded in the backside Cu layer of the DBC. Pautsch et al. [15] analyzed a double sided microchannel cooling embedded in AlSiC plate below a silicon power device and predicted 26% over single sided cooling devices. Standalone jet impingement studies have been documented for characterization of jet geometry in terms of HTCs and Reynold's number (Re) [16]. Additional techniques studied for power electronics cooling include immersion cooling [17] and nanofluid cooling [18].

In the present work single phase cooling techniques were chosen to be integrated with the AlSiC heat sink described earlier. Three approaches for heat transfer enhancement was investigated to reduce the convective thermal resistance, namely single phase flow through minichannels, single phase flow through pin fins and pin fins with jet impingement cooling. For initial comparison, the approaches were compared at a fixed pumping power. The use of pumping power (W_{pump}) as a governing metric is justified, because as shown in Eq. (1), it implicitly governs the mass flow rate of the coolant denoted by \dot{m}_{tot} and the induced pressure drop (ΔP) as a result of this flow simultaneously. The density of fluid is denoted by ρ . As the mass flow rate and pressure drop are intimately coupled, the cooling system design based on independent design limitations on both these variables is often complicated.

$$W_{Pump} = \frac{\Delta P \times m_{tot}}{\rho} \tag{1}$$

Analytical calculations were performed to investigate the effect of design parameters, such as channel size and aspect ratio, pin size and spacing, and jet diameter on variation of HTC on the backside of the base plate and ΔP for a fixed pumping power. These calculations aided in the selection of design variables for each of the cooling scenarios that led to the best possible heat removal for each technique.

For the next part of the analysis, 3-D models of the package with the stacking shown in Fig. 1(b) and parameters selected from the analytical study were developed, and CFD simulations were conducted in ANSYS FLUENTTM. This study was performed to observe the effect of coupled heat spreading and fluid flow on device temperatures with the new AlSiC baseplate/heat sinks. Finally, a detailed comparison among all methodologies was performed to determine the relative differences in the various cooling methods. In this fashion, the competitive advantage of the present design over DBC-based designs was retained in terms of heat dissipated per unit mass of the package and its reliability. The novelty of this work lies in the design of AlN - AlSiC low CTE based packaging combined with heat transfer enhancement features which allow it to perform similarly to copper based cooling designs from a thermal perspective.

2. PARAMETRIC STUDIES ON ALSIC BASEPLATE THICKNESS

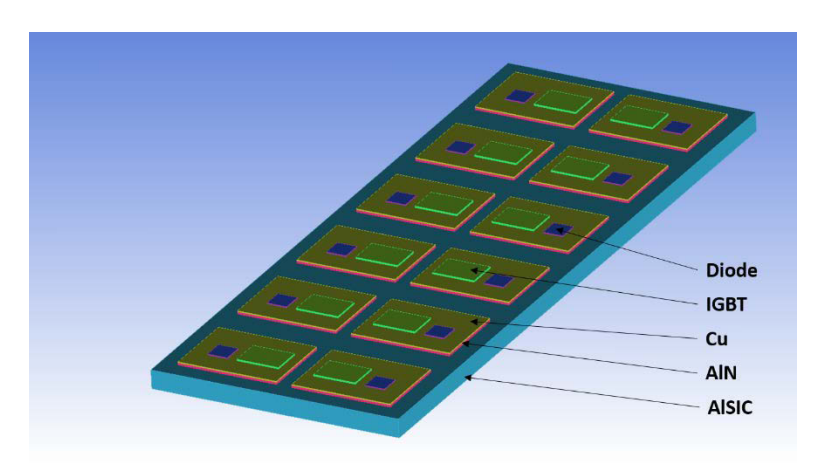


Figure 2. Toyota Prius inverter geometry dissipating 2400 W.

For a model system, the power electronics component of a Toyota Prius inverter was integrated with the Cu-AIN-AISiC and modeled with the geometry as shown in Fig. 2 and material layer sequence as shown in Fig. 1(b) [19]. The Toyota Prius design was chosen or a one-on-one comparison of device temperatures and heat spreading with the new package. The conventional power electronic package dissipates 2400 W through 12 pairs of an integrated gate bipolar transistor (IGBT) device and a diode. Each IGBT dissipates 120 W cm⁻², whereas each diode dissipates 95 W cm⁻², leading to a 200 W total heat dissipated by a pair of an IGBT and a diode. While not all IGBTs and diodes may be dissipating heat at the same time, they are assumed to do so in the present work, as this is comparative exercise. Table 2 shows the summary of the operating conditions and thicknesses of the individual layers used in the steady state thermal simulations, which are adapted from the work by Malu, Bora, Nakanekar and Tonapi [19]. The footprint of the devices and the rest of the material layers remained the same as the original geometry, the details of which are described in the work by Malu, Bora, Nakanekar and Tonapi [19].

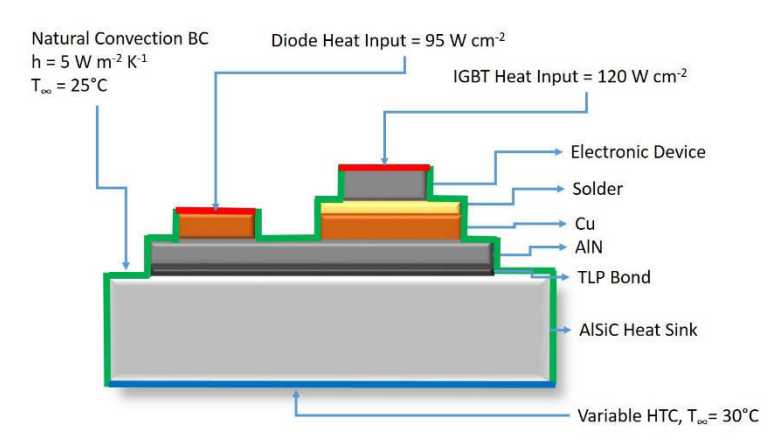


Figure 3. Boundary conditions applied on the exposed surfaces for the parametric study to determine the optimum thickness of AlSiC baseplate. This figure shows a pair of IGBT and a diode of the 12 pairs shown in Figure 2.

Table 2. Details of material layers in the modified package.

Layer	Thickness (mm)	Thermal Conductivity
		$(W m^{-1} K^{-1})$
Diode	0.32	120
IGBT	0.51	120
Solder	0.10	50
Copper	0.41	401
AlN	0.64	155
TLP Bond	0.10	133
Baseplate	3.00	170 – AlSiC
_	6.00	
	9.00	

As shown in Fig. 3, a range of convection HTCs at 30°C was applied on the backside of the AlSiC heat sink and the maximum device temperature was noted for each of these simulations. Although 30°C was not a realistic value of the coolant inlet temperature for automotive applications, it was chosen for this set of simulations for a one-to-one comparison with the conventional module studied by Malu, Bora, Nakanekar and Tonapi [19]. Furthermore, while detailed fluid flow modeling accounting for coolant heating are described in the later section, this study of thermal modeling was conducted to analyze the effect of AlSiC layer thickness on device temperature only. For the surfaces that were exposed to the ambient, a constant HTC of 5 W m⁻² K⁻¹ was assumed. The radiation becomes significant, when

temperature of the surface is high and natural convection is the predominant convection mode. In this case, however the heat removal is dominated by how effectively the heat transferred from the device to the heat sink, where the heat transfer coefficient values considered in the simulation were greater than 10000 W m⁻² K⁻¹. Approaching this problem from the resistance network standpoint, the addition of radiation heat transfer from the exposed surfaces would reduce their heat transfer resistance by nearly up to 2.6 times, however despite this change in the resistance, the surface resistance is still significantly larger than the conduction resistances of the material layers and that of the convection heat transfer from the heat sink. For comparison, the least conductive material layer is AlSiC with the thermal conductance at 56000 W m⁻² K⁻¹ when compared with 5 W/m² K⁻¹ with only convection and 13 W m⁻² K⁻¹ with convection and radiation. So, the heat generated in the device finds a much easier way through the conducing material layers and fluid flow through the heat sink. Hence, radiation heat transfer is neglected in the simulations. The geometrical models were developed and meshed in ANSYS ICEMCFDTM and steady state simulations were carried out using ANSYS FLUENTTM platform. The simulations were checked for mesh independence and energy conservation equations were solved until they converged within 0.5%. Sample temperature contours are shown in Fig. 4 for the case with a 3 mm AlSiC baseplate applied with an HTC of 40 kW m⁻² K⁻¹, where the IGBT temperatures were seen to rise to 66°C, compared to the coolant temperature of 30°C. This results in a ΔT_{Max} (the difference between the maximum device temperatures and coolant temperature) of 36°C.

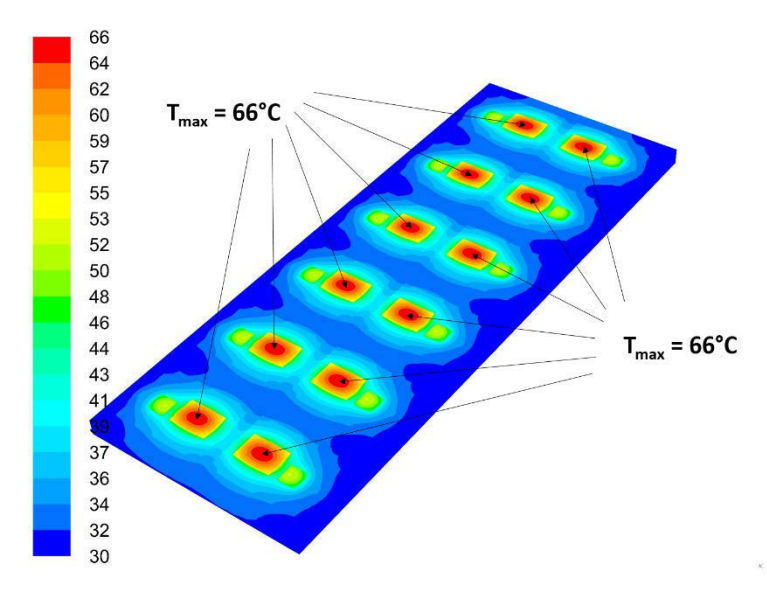


Figure 4. Sample temperature contours with the TLP bond with 3 mm AlSiC heat sink with an HTC of 40 kW m⁻² K⁻¹.

An interesting pattern was observed, when simulations were conducted for different AlSiC thicknesses with varying HTCs. The differences between the maximum device temperatures and coolant temperature ($\Delta T_{\rm Max}$) were plotted as shown in Fig. 5. For a low HTC value such as 10 kW m⁻² K⁻¹, thick baseplates (9 mm) aided in spreading heat effectively, yielding to lower ΔT_{Max} values compared to their thin counterparts. However, as HTC was increased to 30 kW m⁻² K⁻¹ and beyond, the pattern changed and thin heat sinks started performing better as compared to their thick counterparts. This reversal of trends was clearly due to the change in relative magnitudes of conduction heat transfer resistance in the heat sink and the convection heat transfer resistance applied at the heat sink wall. For low HTCs, the convection heat transfer resistance was large, therefore thicker plates acted as more efficient heat spreaders before heat was removed. On the other hand, for high HTCs applied at the heat sink wall, heat could be readily removed from the system and any additional thickness of the heat sink acted as an additional barrier to heat removal. Therefore, thin heat sinks performed better than thick heat sinks in terms of device temperatures at high HTCs. Furthermore, they were found to be more responsive to the change in HTCs due to reduction of thermal mass in the system. In contrast, the change in device temperature with any change in HTC was found to

be minimal for a 9 mm thick AlSiC plate. The 9 mm thick baseplate and heat sink assembly (Cu baseplate and Al heat sink) beneath the solder attach studied by Malu, Bora, Nakanekar and Tonapi [19] exhibits a similar behavior when HTC values are changed. This means that, for a conventional stack, any major increase in HTC may not yield appreciable decrease in ΔT_{Max} . Using thin heat sinks can result in a compact and inexpensive package.

Another aspect of these simulations was the performance of Cu-AlN-AlSiC design with respect to the conventional Cu – Al base plate – heat sink designs. As shown in Fig. 5 [19], the device temperature rise values in a conventional package reported by Malu, Bora, Nakanekar and Tonapi [19] were between 36°C and 39°C for an HTC range of 10 kW m⁻² K⁻¹ to 20 kW m⁻² K⁻¹. Extrapolating the curves for the conventional package using a hyperbolic function consistent with Newton's law of cooling, an AlSiC heat sink could be competitive with the conventional power electronics package in terms of device temperatures, if a 3 mm plate were used with an HTC of 50 kW m⁻² K⁻¹ and above. It could be argued that extrapolation of the device temperature curves for the conventional device could have the slope consistent with thinner AlSiC plates, yet it has a 6 mm thick Al heat sink in addition to the 3 mm thick Cu base plate. The use of steeper slopes for the conventional devices could have been justified only when a 3 mm Cu heat sink were incorporated in the conventional design without any Al layer, and this was not the case. Furthermore, using a linear extrapolation is not physically consistent and would result in unrealistic device temperature values. Hence, single-phase cooling techniques were investigated analytically and system and geometry parameters that could yield HTCs greater than 50 kW m⁻² K⁻¹ were sought. The thickness of AlSiC heat sink then chosen for the analytical and further computational modeling was 3 mm.

Another argument regarding the thickness of the AlSiC heat sink can be sustained as to why thicknesses smaller than 3 mm were not analyzed. While it is possible to use even thinner AlSiC heat sinks and they may well result in more effective heat removal for a given HTC

consistent with Fig. 5; it is not practical to use such thin AlSiC plates, because the cooling features such microchannels or pin fins are to be embedded within the plate. It is critical to understand that these thermal simulations assume HTC values at the AlSiC wall, however, the coolant flow must be able to generate this high HTC in the heat sink to realize this performance. For instance, as it will be shown later in the article, the minichannels with 2 mm or greater size result in effective fluid flow through the AlSiC heat sink, hence the AlSiC heat sink must be thicker than that to be able to fabricate channels of 2 mm size and still retain its structural rigidity. If 1 mm thick AlSiC heat sinks were to be employed, channels smaller than 1 mm would have to be carved in the AlSiC plate, which in turn worsens the heat removal performance. Therefore, in this set of simulations AlSiC plates thinner than 3 mm were not simulated.

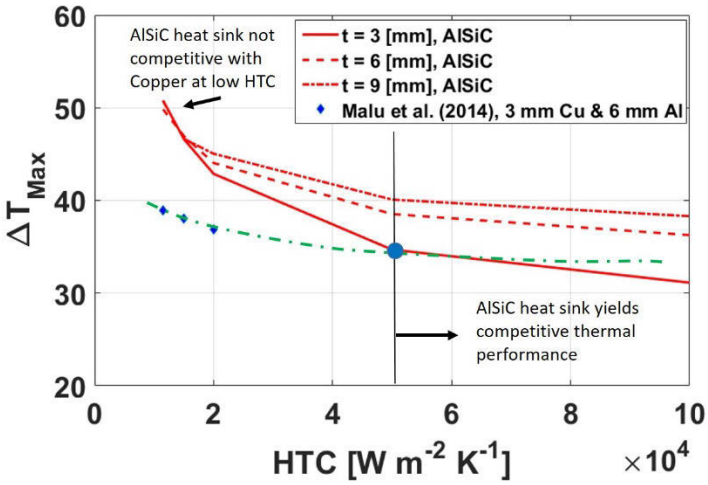


Figure 5. Variation of the difference between device temperature and fluid temperature (ΔT_{Max}) with HTCs for different thicknesses.

3. ANALYTICAL MODELING

The parametric studies conducted in the present work were based on a Toyota Prius inverter geometry [19] as shown in Fig. 6(a), which also shows one of the identical sections of the complete module. Each pair of an IGBT and a diode dissipates 200 W and a set of two pairs, or the identical section as shown in Fig. 6(b), dissipates 400 W.

For the direction of the coolant flow as shown in Fig. 6(b), any of the six sets of electronic device pairs, which dissipate 400 W, can be viewed as the domain of interest. This simplification avoided the computational cost and time of simulating the entire package. The direction of the flow of coolant is also shown. This direction was chosen to minimize the pressure drop and to limit the temperature rise of the coolant while flowing through the package. The pumping power assumed for the analytical calculations for channel flow and pin fin flow was 8 W, which is 2% of the total heat dissipated by the two pairs. This value was taken as 4 W for jet impingement, wherein the flow of coolant was assumed to be perpendicular to the surface of the substrate, and only one IGBT-diode pair is sufficient to describe the temperature distribution and heat spreading. This value of pumping power was estimated based on an independent exercise that studied the effect of coolant mass flow rate on pumping power and pressure drop, simultaneously trading it off with HTCs and is described in a later section. This pumping power as shown in Eq. (1) is a function of mass flow rate, $\dot{m}_{\rm dot}$ and pressure drop, ΔP through the system. With Eq. (1), the efficacy of any geometry can be assessed independently based on how small the pressure drop is for any given mass flow rate.

The coolant considered in the present work is a mixture of water and ethylene glycol (50/50) and was selected for its broad range of operating temperatures. The inlet coolant temperature was considered to be 80°C and the fluid properties, such as density, ρ , viscosity, μ , specific heat, c_p and and thermal conductivity, k, were evaluated at this temperature [20].

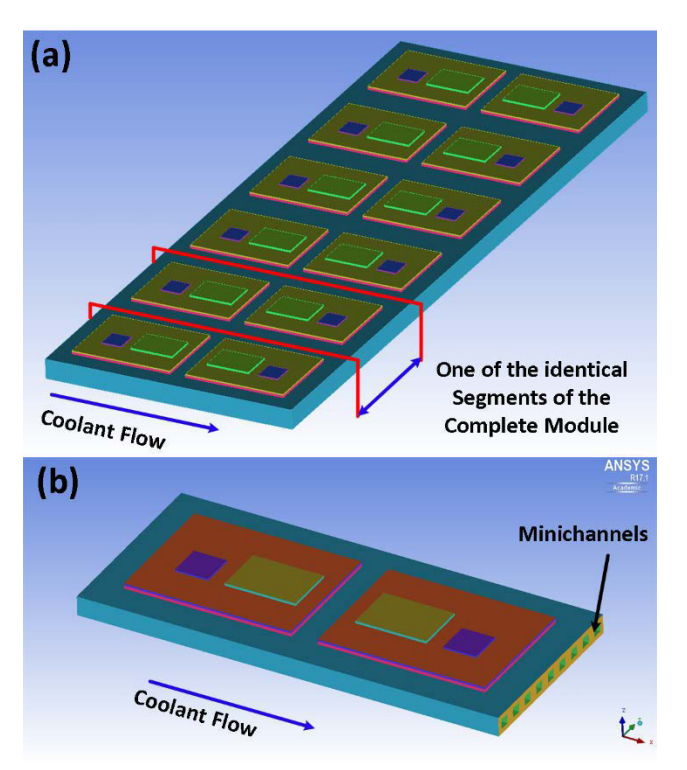


Figure 6. (a) Schematic showing an identical segment of a Toyota Prius inverter dissipating 400W (b) Magnified view of the identical segment selected for simulations also showing minichannels.

1.1. Channel cooling

The aspect ratio and the channel width of the channels were considered variables in the calculations for the channel cooling design. The friction factor and the HTC were estimated using Churchill equations shown in Eqs. (2) through (4) [21, 22]. The effect of aspect ratio, a, hydraulic diameter D_h , surface roughen eps, Reynolds number, Re and Prandtl number, Pr on Nusselt number, Nu and friction factor, f were taken into account. The details of the geometry and other factors considered for analytical modeling of channels are shown in Fig. 7.

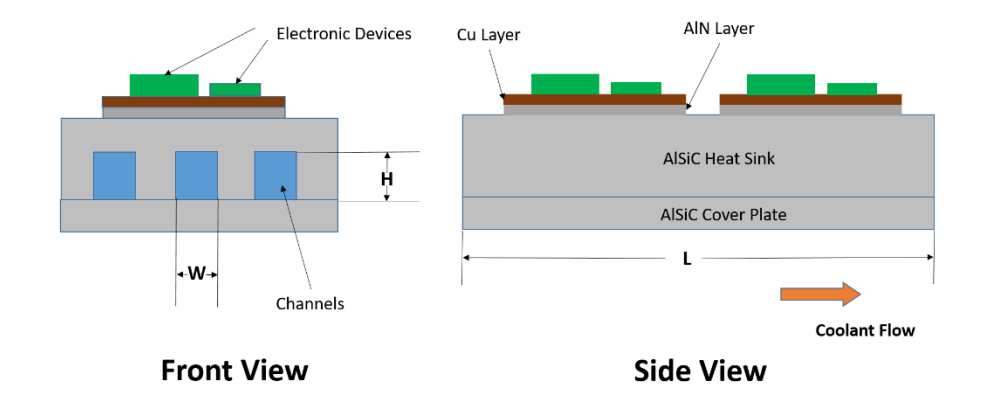


Figure 7. Schematic showing the geometry parameters and arrangement of layers considered for modeling channel flows.

$$f = 8 \cdot \left(\left(\frac{8}{\text{Re}} \right)^{12} + \left[\left(\frac{37530}{\text{Re}} \right)^{16} + \left(-2.457 \cdot \ln \left(\left[\frac{7}{\text{Re}} \right]^{0.9} + 0.27 \times \frac{eps}{D_h} \right) \right)^{16} \right]^{(-1.5)} \right)^{(-1.5)}$$
(2)

$$a = \frac{W}{H}$$

$$Nu_o = -0.013 \times \left(\frac{1}{a}\right)^2 + 0.52 \times \left(\frac{1}{a}\right) + 2.8$$
(3)

$$\left(\frac{D_h \times HTC}{k_g}\right)^{10} = \left(Nu_0\right)^{10} + \left[\frac{e^{\frac{(2200-Re)}{365}}}{\left(Nu_0\right)^2} + \left(\frac{1}{Nu_0 + \frac{0.079Re\sqrt{f} \text{ Pr}}{\left(1 + Pr^{4/5}\right)^{5/6}}}\right)^2\right]^{-5} \tag{4}$$

The pressure drop components in the package consisted of contraction at the channel inlet, friction at the channel wall and sudden expansion at the channel exit. Respectively, these components were calculated as shown on the right hand side (RHS) of Eq. (5) [23]. In these equations, V is the channel velocity and $V_{\rm in}$ the header velocity.

$$P_{in} + \frac{\rho V_{in}^{2}}{2} = 0.5 \times \frac{\rho V^{2}}{2} + f \frac{L}{D_{h}} \frac{\rho V^{2}}{2} + 0.5625 \times \frac{\rho V^{2}}{2} + P_{atm}$$

$$\Delta P = P_{in} - P_{atm}$$
(5)

These equations, when solved together with Eq. (1), yielded HTC and ΔP as a function of channel width and aspect ratio. By independently varying channel width from 0.4 mm to 2.0 mm and aspect ratio from 0.1 to 1, HTC and ΔP were mapped as shown in Fig. 8(a) and 8(b) respectively. Note that the aspect ratio values below a certain threshold for larger channels were not analyzed, as the height of the channel, H was assumed to be limited to 2 mm and width, W is allowed to vary. The height was limited to 2 mm, because as described earlier the total height/thickness of the AlSiC heat sink was selected as 3 mm.

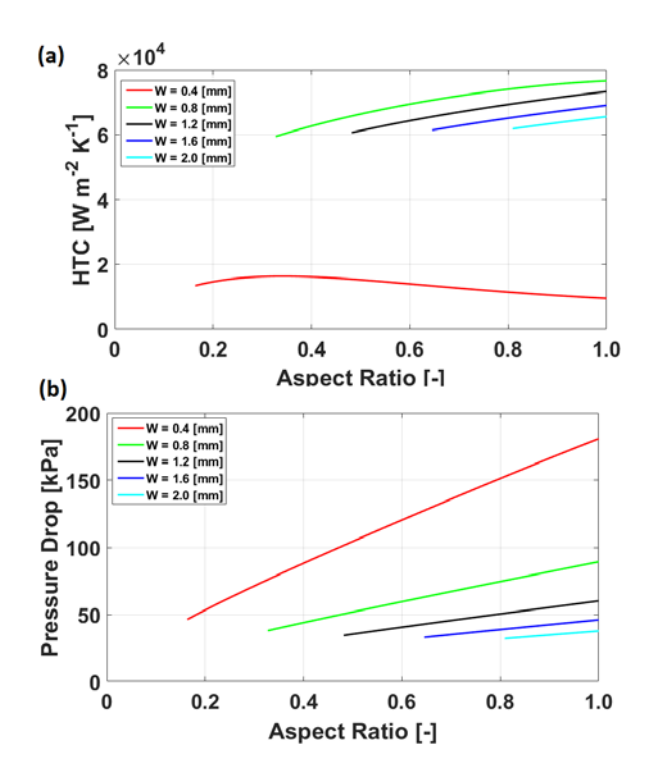


Figure 8. (a) HTC (b) ΔP variation with aspect ratio and channel width.

For the smallest channel size of 0.4 mm, the coolant flow was laminar, and therefore the HTC was at least 75% smaller than those obtained with larger channels. As channel size increased, it could carry more coolant with a small ΔP . For turbulent flow through minichannels, HTCs greater than 60 kW m⁻² K⁻¹ were achievable at the ΔP smaller than 40 kPa. Therefore, a square channel with a width of 2 mm was selected for the CFD/HT simulation to predict the device temperature using this cooling scheme. This geometry yielded an HTC of 65 kW m⁻² K⁻¹

¹ and a ΔP of 40 kPa with a mass flow rate of 0.2 kg s⁻¹. Figure 6(b) shows the minichannels embedded in the AlSiC heat sink with a square cross section of side 2 mm.

It must be noted that bigger channels might have yielded a better HTC, as compared to the 2 mm case, because they can carry more coolant with smaller pressure drop. However, this would have then required a thicker AlSiC plate in the first place. However, as shown in Figure 5, the use of a thicker AlSiC plate would have required a greater HTC to be then competitive with the Cu base plate, negating any potential benefit that would have be achieved by making larger channels. Furthermore, increased thickness of the AlSiC plate results in more material, more cost and weight to fabricate the package with analogous thermal performance. Hence, the use of 2 mm minichannels is justified.

1.2. Pin fin cooling

Pin fins provide additional surface area for heat spreading and rejection, thereby requiring small temperature difference between the coolant and the surface to be cooled. The analysis becomes complicated, when pumping power becomes the deciding factor, as excessive pressure drop for the flow through pins can severely decrease the mass flow rate and HTC at the pin fin surface. Zukauskas correlations shown in Eqs. (6) through (8) were used to calculate the HTC and ΔP over the pins. A staggered pin arrangement was chosen and appropriate equations for constants C_2 and C were applied, depending on the number of pin fin rows and Re. For determination of K and f in Eq. (8), curve fitted planes as functions of fin spacing S_T and fin diameter, D were determined and incorporated [24]. These geometry parameters and their locations within the considered geometry for pin fin cooling are shown in Fig. 9.

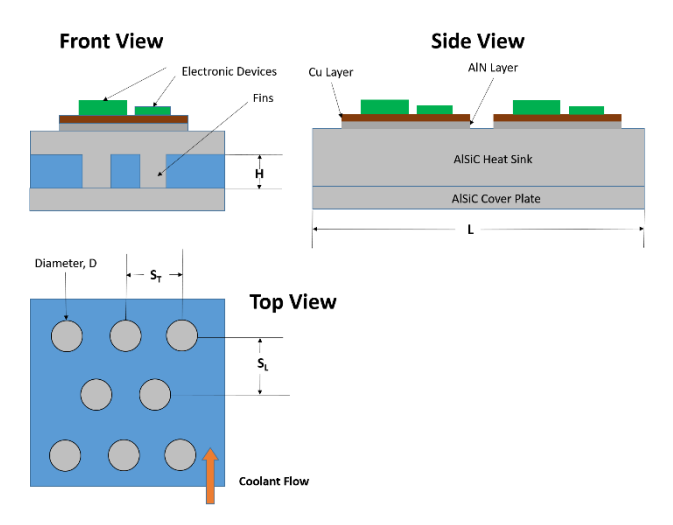


Figure 9. Schematic showing the geometry parameters and arrangement of layers considered for modeling flow over pin fins.

$$V_{Max} = V_{Inlet} \frac{S_T}{S_T - D}$$

$$Re_{D,Max} = \frac{\rho V_{Max} D}{\mu}$$
(6)

$$Nu = \frac{HTC \times D}{k} = C_2 \times C \times \text{Re}_{D,Max} \times \text{Pr}^{0.36}$$
(7)

$$\Delta P = f \frac{L}{D_h} \frac{\rho V^2}{2} K \tag{8}$$

Figure 10 shows analogous spectra of HTC and ΔP for the pin fin flows. The diameter, D is varied from 0.5 to 3 mm, whereas two pin heights, 1.0 mm and 1.5 mm, were chosen for analytical calculations, whereas $S_{\rm T}$ and $S_{\rm L}$, the lateral and axial pin fin pitch values were varied from 1.25 mm to 5.0 mm. The pin fin height is again consistent with the maximum thickness of the AlSiC plate of 3 mm and has a similar justification as in case of the channels.

The HTC values obtained with the pumping power of 8 W with pin fins peaked at 60 kW m⁻² K⁻¹ as shown in Fig. 10(a), because of high pressure drop offered to the flow of the coolant as shown in Fig. 10(b). For this geometry, increase in pitch values resulted in a reduced resistance to the flow and a reduced ΔP , however the HTC values did not improve despite this

increase in mass flow rate. This is because, HTC values for pin fins are a strong function of total surface area available for heat transfer, which decreased as fin pitch and diameter increased. The total base surface area was constant; hence, any increase in D and and S_T and S_L results in a small number of rows and columns, in turn, small surface area available for heat transfer. A similar logic can be applied for describing the effect of fin height on HTC and ΔP .

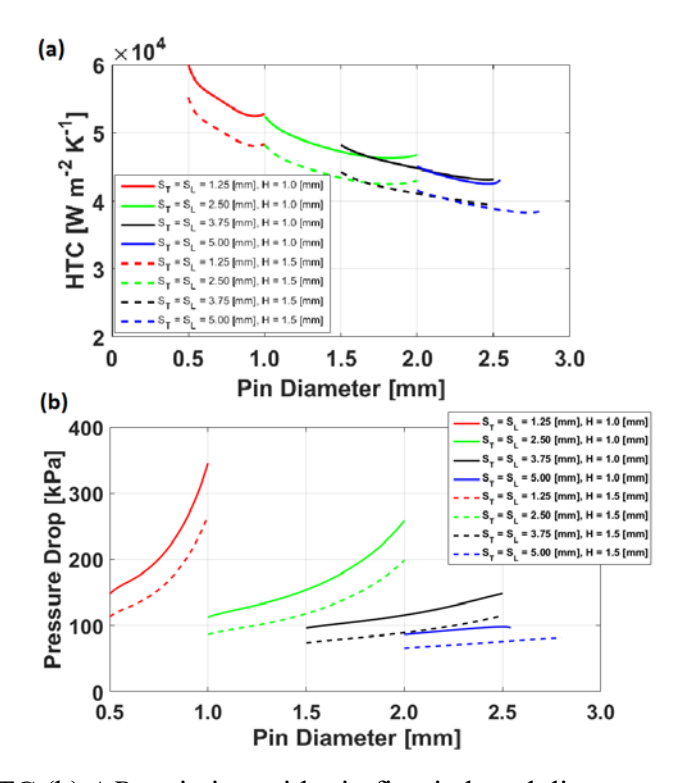


Figure 10. (a) HTC (b) ΔP variation with pin fin pitch and diameter.

Therefore, unlike the channel flow, reduced ΔP cases for pin fins at a constant pumping power did not result in improvement in HTC values. The best possible scenario for computational simulation then was the pin diameter of 0.5 mm and pitch values of 1.25 mm and pin height of 1.0 mm. This combination resulted in a ΔP of 146 kPa, while yielding an HTC of $60 \text{ kW m}^{-2} \text{ K}^{-1}$. The mass flow rate corresponding to this set of parameters was 0.053 kg s⁻¹.

Figure 11(a) shows the assembly of the power electronic package and the pin fin assembly attached at the bottom of the AlSiC layer. Although Fig. 11(b) shows the pin fin assembly separately, pin fins can be fabricated as an integral part of the AlSiC material layer,

by melting a mirror mold of the fins from the bottom side. The pin fin diameter, fin pitch and heights shown in Fig. 11(b) are those mentioned in the previous paragraph.

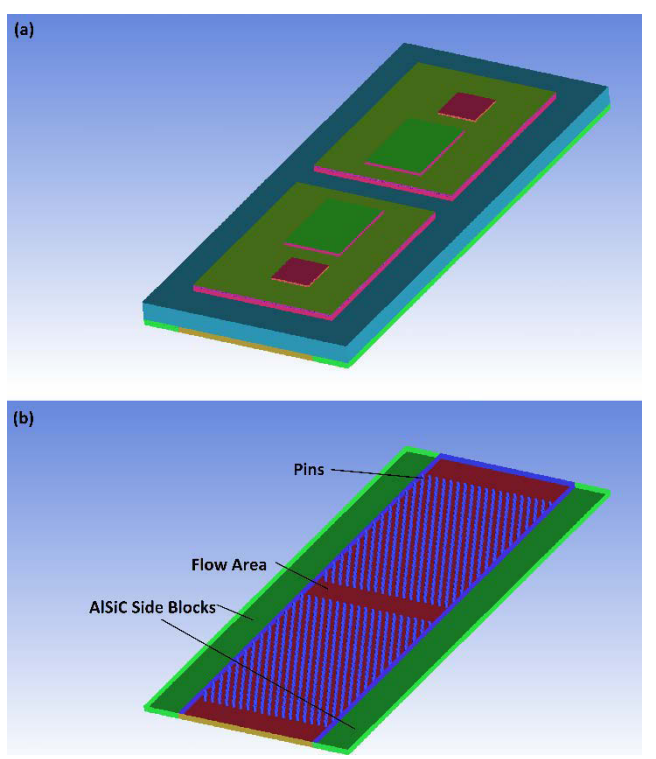


Figure 11. (a) Complete assembly of power package with pin fin assembly attached at the bottom of AlSiC plate (b) Pin fin assembly (pins in blue) showing flow region in the red. Flow cross sectional area is smaller than the total area, because pin fins on the sides are not found to aid in heat spreading and are therefore not needed.

1.3. Spray or jet cooling

For the analytical model of the spray cooling scheme, a single pair of an IGBT and a diode was sufficient, as the flow of the coolant was normal to the base surface. The results from a single inlet stream could be easily applied to the other stream in the package shown in Fig. 2. Figure 12 shows the schematic of the package and jet manifold assembly used for analytical calculations and computational simulations, whereas Fig. 13 shows the details of the geometry and schematic of the overall domain. The coolant flowed from the inlet manifold to several rows of jets. It was then directed on to the target surface or the backside of the AlSiC plate. At the target surface, the coolant stream bent by 90° and then exited the zone. The pressure drop components encountered for the coolant flow were that at the jet constriction, friction in the jet

body, sudden expansion in the cooling zone, bending of the flow, and friction to the flow through cooling zone were calculated as shown in the right hand side of Eq. (9). [10, 23].

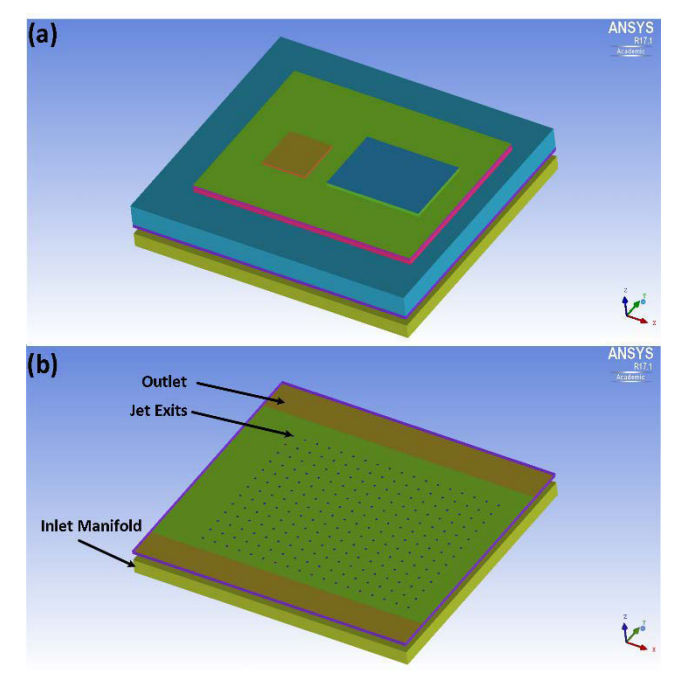


Figure 12. (a) Schematic o the complete geometry used for spray cooling (b) Jet array inlet manifold assembly.

$$P_{in} + \frac{\rho V_{in}^{2}}{2} = 0.5 \times \frac{\rho V_{j}^{2}}{2} + f \frac{L_{j}}{D_{h}} \frac{\rho V_{j}^{2}}{2} + f \frac{W}{2} \frac{\rho V_{out}^{2}}{2} + f \frac{\rho V_{out}^{2}}{2} + f \frac{W}{2} \frac{\rho V_{out}^{2}}{2} + P_{atm}$$

$$\Delta P_{Total} = P_{in} - P_{atm}$$
(9)

Equations (10) through (14) were used to estimate HTCs achievable by the jet array cooling as a function of jet spacing S, jet diameter D, distance between jet exit and the target surface H. These parameters were varied in the present work to determine the best possible cooling scenario.

Front View Electronic Devices AlSiC Heat Sink Jet Length Jet Stream Direction Top View

Figure 13. Schematic showing the geometry parameters and arrangement of layers considered for modeling jet impingement.

$$A_r = \frac{\pi D^2}{4S^2} \tag{10}$$

$$G = 2 * A_r^{0.5} \left[\frac{1 - 2.2 \times A_r^{0.5}}{1 + 0.2 \left(\frac{H}{D} - 6 \right) \times A_r^{0.5}} \right]$$
 (11)

$$F = \frac{\text{Re}^{0.667}}{2} \tag{12}$$

$$K = \left[1 + \left(\frac{H/D}{0.6/A_r^{0.5}} \right)^6 \right]^{-0.05}$$
 (13)

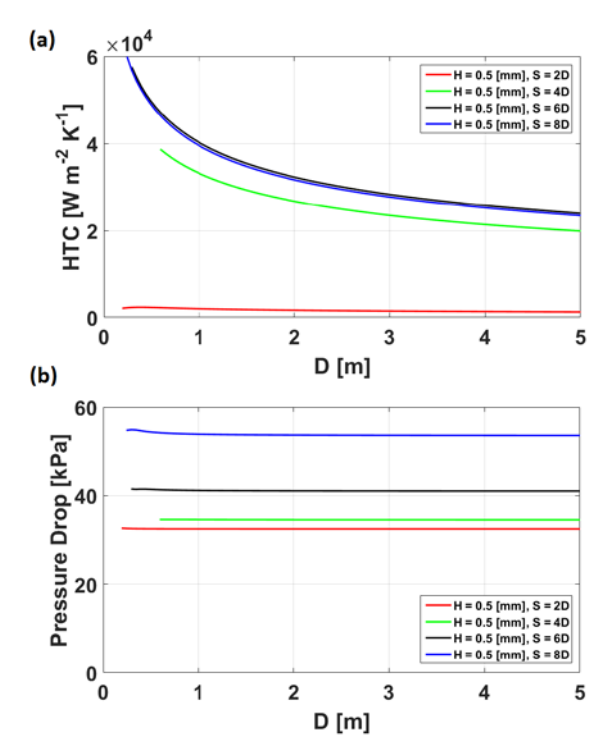


Figure 14. (a) HTC (b) ΔP variation with jet spacing S, D, and H.

$$Nu = \frac{HTC \times D}{k} = G \times F \times K \times \Pr^{0.42}$$
(14)

Figure 14 shows the variation of HTC and ΔP as a function of S, D and H. Three different H values, 0.5 mm, 1.0 mm and 1.5 mm were analyzed; however, results with only 0.5 mm are described here for brevity and them being better than the other two. As shown in Fig. 15(a), HTC value achievable with a power of 4 W and with the smallest jet diameter of 0.3 mm was 57 kW m⁻² K⁻¹ and a jet spacing of 1.8 mm. The corresponding value of pressure drop is 41 kPa as seen in Fig. 15(b) and the mass flow rate is 0.094 kg s⁻¹, which were chosen for the computational investigation.

Overall, it can be inferred that optimized geometries of channels, pin fins and jets for a given constant pumping power can yield HTCs above 50000 W m⁻² K⁻¹ and thereby create the possibility of achieving a competitive performance to Cu base plates, when employed to cool the power electronic package. Table 3 shows the summary of the analytical modeling results.

Table 3. Summary of the analytical modeling exercise.

Features	Channels	Pins	Jets
Geometry	2 mm square	0.5 mm diameter	0.3 mm jet diameter
		1.0 mm height	1.8 mm pitch
		1.25 mm pitch	0.5 mm jet length
HTC	65000	60000	57000
ΔP	41	146	40
Mass flow	0.2	0.053	0.094
rate			

4. COMPUTATIONAL MODELING

The analytical models in the previous section provided insight into the minichannel, pin fin and jet geometries that yielded the best individual cooling performances. Next, the computational investigation to predict heat spreading in the substrate and the subsequently the temperature of the device was conducted with these three geometries.

With the coolant mass flow rates mentioned in the preceding sections and Table 3 and the material layers defined in Table 2, the natural convection heat transfer coefficient for the surfaces exposed to ambient was assumed to be 5 W m⁻² K⁻¹ as in case of thermal simulations described in a previous section. For the computational simulations, all the boundary conditions are the same as shown in Figure 3, except the additional fluid flow boundary conditions. The fluid inlet boundary condition is the fixed mass flow rate with the input fluid temperature of 80°C. The fluid outlet boundary conditions is pressure outlet, which assumes that the gauge pressure is zero. The geometries were built and meshed in ANSYS ICEMCFDTM and steady state simulations were carried out using ANSYS FLUENTTM platform. The turbulence model selected for the fluid flow analysis was Spalart Allmaras for its robustness and its default parameters in ANSYS FLUENTTM. The simulations were checked for grid independence and the mass, momentum and energy conservation equations are solved until they were converged within 0.5%. Temperature predictions from these simulations can be applied with these generalized error estimates. The heat flux boundary applied at the IGBT and diode surfaces were

120 W cm⁻² and 95 W cm⁻², respectively. The summary of simulation parameters is shown in Table 4 [10]. The coolant is chosen to be water and ethylene glycol mixture (50/50).

Table 4. Fluid boundary conditions and channel geometry details selected for modeling the heat spreading and removal.

the new spreading and reme van			
Parameter	Value		
Total heat dissipated	400 W		
IGBT heat flux	120 W cm ⁻²		
Diode heat flux	95 W cm ⁻²		
Coolant	Water - ethylene glycol		
Coolant density	999 kg m ⁻³		
Coolant specific heat	3820 J kg ⁻¹ K ⁻¹		
Coolant conductivity	0.391 W m ⁻¹ K ⁻¹		
Coolant viscosity	0.0011 N s ⁻¹ m ⁻¹		
Coolant inlet temperature	80°C		
Coolant Pumping power	8 W		
Minichannel cross section	$2 \text{ mm} \times 2 \text{ mm}$		
Coolant mass flow rate - channels	0.2 kg s ⁻¹		
Pin fin diameter	0.5 mm		
Fin pitch	1.25 mm		
Fin height	1 mm		
Coolant mass flow rate - fins	0.053 kg s^{-1}		
Jet diameter	0.3 mm		
Jet spacing	1.8 mm		
Jet – target surface gap	0.5 mm		
Total mass flow rate - jets	$0.094~{ m kg~s^{-1}}$		

Figure 15(a) shows the temperature contours for the plane parallel to the coolant flow at the minichannel centroid. AlSiC body temperatures adjacent to the channels up to 94°C were observed, while a gradual increase in temperature up to 1°C was seen as coolant flowed through channels and picked up heat. Coolant flowing through the manifold at low velocity could be seen accelerating at the channel entrance reaching velocities of up to 8 m s⁻¹ in Fig. 15(b). This velocity was responsible for generating the HTC of 65 W m⁻² K⁻¹ at the channel side walls and the maximum device temperature of 116°C or a ΔT_{Max} of 36°C. At the exit of the channels in the manifold, jets could be seen as a result of channels emptying the coolant in the exit manifold. Pressure contours as shown in Fig. 15(c) also correspond to the same flow pattern. Pressure drop due to sudden contraction at the channel entrance, negative pressure at the channel exit followed

by pressure recovery at the manifold exit as seen in Fig. 15(c) were also observed in the analytical calculations. The interplay between increased velocity and decreased pressure was accurately captured by these simulations. While the pressure at the channel outlet becomes negative, it does not mean that the flow direction is reversed. The pressure at the outlet of the assembly is assumed to be atmospheric and the outlet header has a greater cross sectional area than the channel size. Hence, the pressure values at all locations adjust themselves depending on corresponding velocities. Qualitatively, the velocity of the coolant through the inlet header is small, followed by acceleration in the channels and the deceleration in the outlet header, which is consistent with Bernoulli's principle.

Additionally, the total ΔP of 40 kPa was in agreement with the analytical value of 40 kPa indicated in Fig. 8(b).

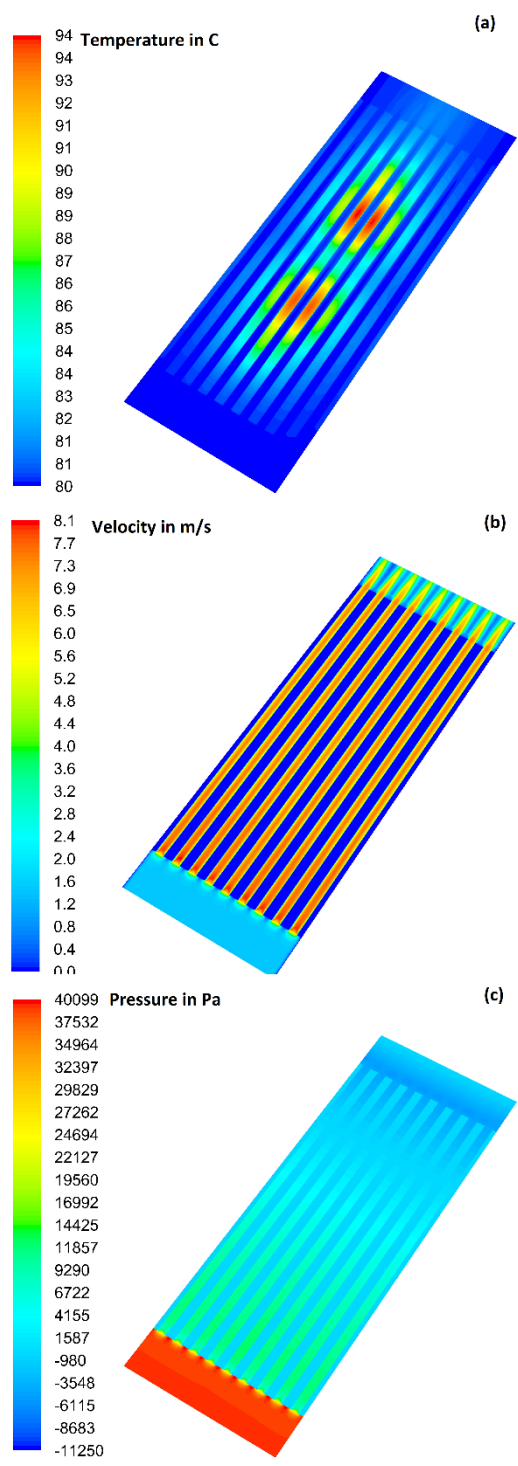


Figure 15. (a) Temperature (b) Velocity (c) Pressure contours parallel to channel flow at the minichannel centroid.

Similar contours are plotted for coolant flow over pin fins in Fig. 16. Unlike local hot spots below the IGBT devices for minichannel flows, pin fin hot spots were larger. The temperature locally within the downstream pins reached up to 88°C as shown in Fig. 16(a). Coolant was seen to significantly warm near the exit with a rise greater than 3°C. Overall, this

resulted in a ΔT_{Max} of 38°C. This was attributed to small coolant flow rate, which was determined by analytical calculations. The velocity profiles in Fig. 16(b) showed a uniform pattern with significant variation around pin fins only, where the flow contracts and expands repeatedly. Although much of the bulk velocity remained as small as 2 m s⁻¹, it reached up to 7 m s⁻¹ at corners and flow contractions around pin fins. Despite these low velocities and low flow rate, pressure contours shown in Fig. 16(c) suggest that the pressure drop over these pins was significantly greater than that in the channels with the total ΔP up to 130 kPa. This value matched satisfactorily with the predicted value of 146 kPa in the analytical calculations.

Finally, fluid flow in a jet impingement scenario was more complicated than the previous two due to multiple bends and contractions. As shown in Fig. 17(a), the cross section parallel to the fluid flow includes the source device/IGBT, thereby showing the maximum temperature as 120°C or the ΔT_{Max} of 40°C. Figure 17(b) and (c) illustrate the fluid flow more clearly, as coolant could be seen entering the jet body and imparting on the backside of the AlSiC plate with velocities as high as 8 m s⁻¹. The selection of jet diameter and spacing via analytical calculations made sure that the jet core made contact with the AlSiC, thereby maximizing the cooling effect. Local variation in the jet velocity as a result of pressure variation in the cooling space was also observed. As the fluid outlets were located on either side of the cross section, the coolant stream flowed from the center of the cooling space toward the sides for removal. It means that the pressure at the center was greater than that at the sides to facilitate this flow. Such variation impacted the local jet exit velocities as each jet body saw different ΔP s across its entrance and exit. Specifically, jets near the fluid exit went through a larger ΔP than those near the center, resulting in high coolant velocities. Despite these local velocity variations not being accounted for in the analytical calculations, the total ΔP value of 39 kPa in the computational simulation matched well with the 41 kPa estimated by the analytical calculations.

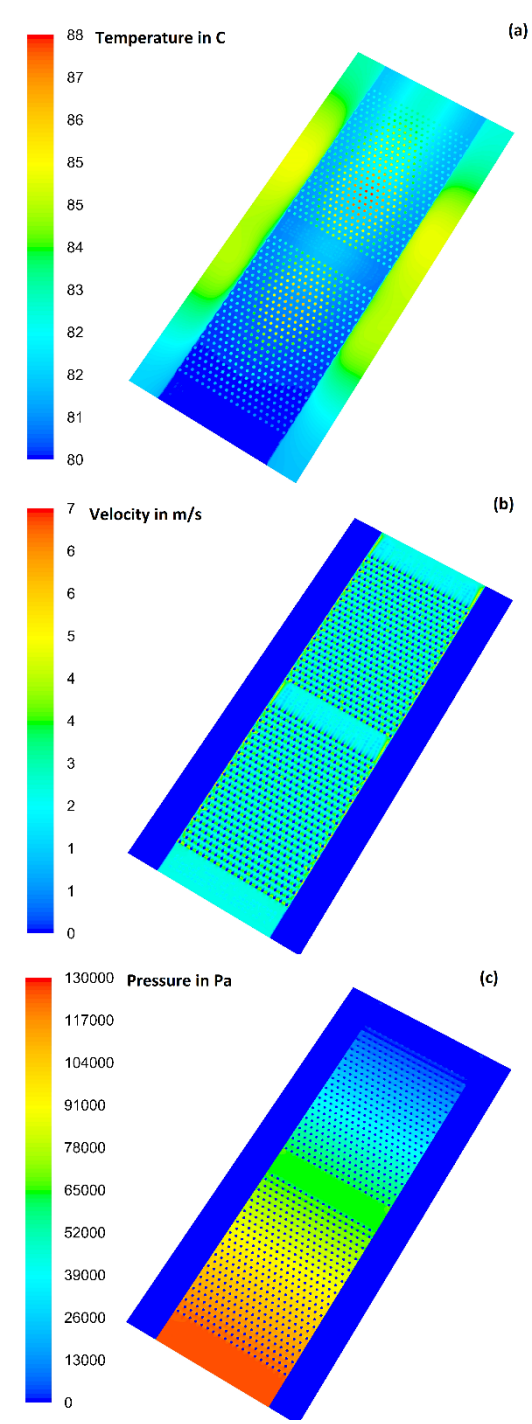


Figure 16. (a) Temperature (b) Velocity (c) Pressure contours parallel to fluid flow at the pin fin centroid.

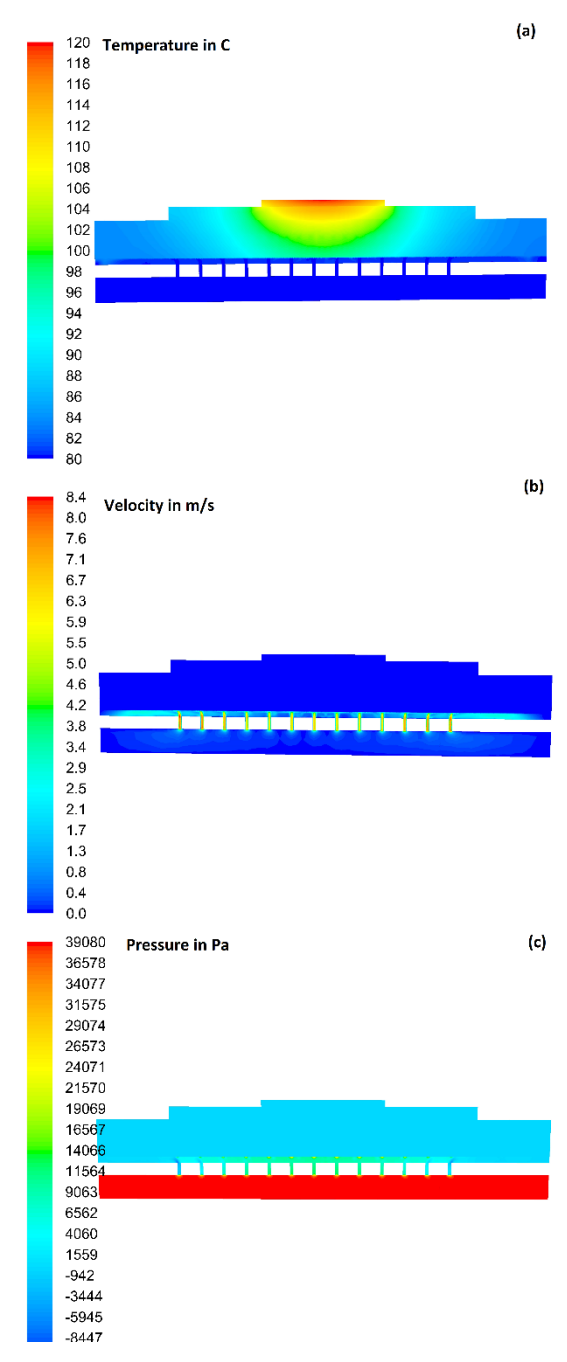


Figure 17. (a) Temperature (b) Velocity (c) Pressure contours parallel to fluid flow in spray cooling scenario (perpendicular to the heat source device).

Figures 18(a), (b) and (c) show the device temperature contours for the channel cooling, pin fin cooling and jet array or spray cooling, respectively.

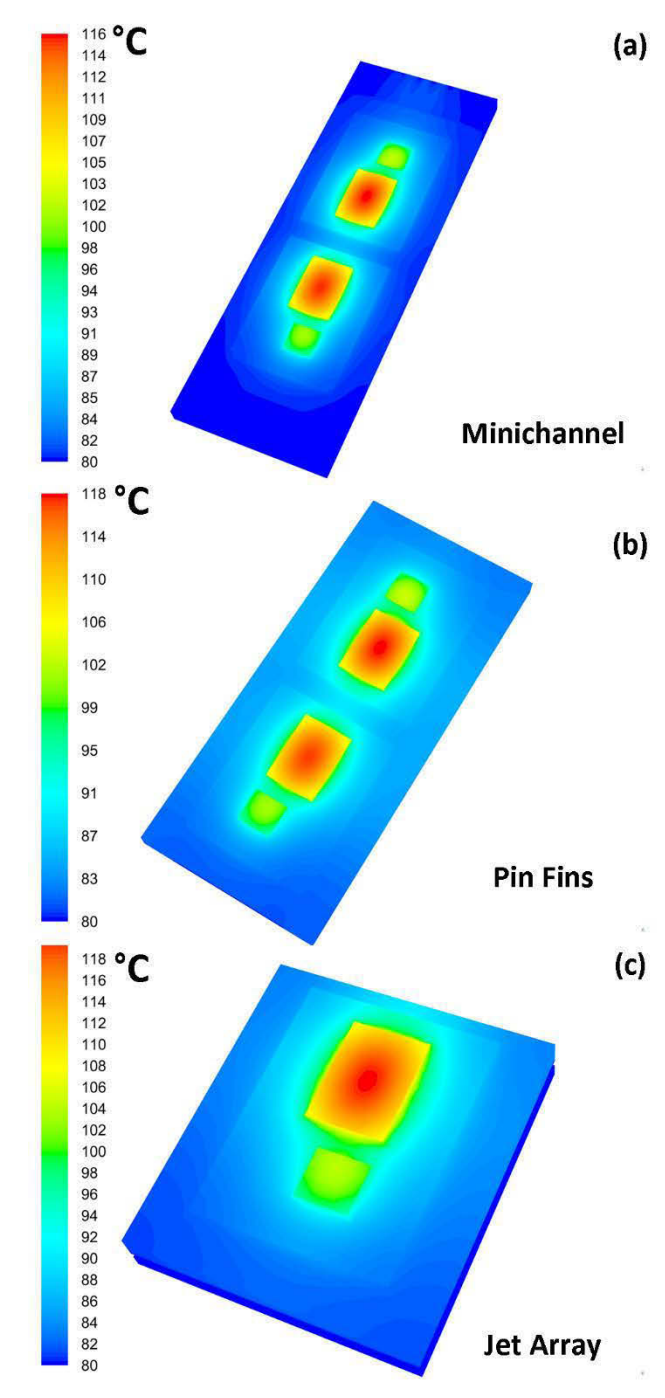


Figure 18. Temperature contours for (a) channel cooling (b) pin fin cooling (c) jet array cooling.

As shown in Fig. 18, $\Delta T_{\rm Max}$ for the channel-cooling scenario was found to be 36°C, while that for the pin fins and jets was found to be 38°C ad 40°C. These temperature rise values are competitive with the conventional Cu-Al based heat sink design and therefore it can be concluded that all three methods, channels, pin fins and jets can lead to similar cooling

performances for a fixed pumping power and can be strong candidates to design an integrated AlSiC heat sink for this new package.

The important inference from this part of the study was that all three techniques can achieve competitive performance to yield an HTC above 50000 W m⁻² K⁻¹, thereby leading to competitive ΔT_{Max} values with Cu-baseplates. However, the pumping power chosen is also a critical factor in this result. The set of operating conditions with a pumping power of 2% of heat dissipated resulted in good heat transfer and pressure drop scenarios, specifically for the minichannel geometry. However, it is opportune at this stage to evaluate, if the 4 W pumping power was indeed able to generate the best cooling scenario for the system. Therefore, with the available set of analytical equations, the pumping power and the mass flow rate were allowed to vary with a fixed minichannel side of 2 mm square. Because mass flow rate and ΔP were directly coupled with HTC through the analytical approach, it was possible to further understand the effect of change of HTC on ΔT_{Max} through computational simulations. This analysis was analogous to that shown in Fig. 5, except that a minichannel geometry was incorporated in computational simulations for very large values of HTC and mass flow rates and pumping power values could be correlated with ΔT_{Max} .

As shown in Fig. 19, the performance enhancement of the cooling system (for any geometry in general) diminishes as HTC increases beyond a certain limit. This was apparent, as drop in ΔT_{Max} was only 3°C for a considerably large increase in HTC from 10⁵ to 10⁶ W m⁻² K⁻¹. Contrary to this small drop in ΔT_{Max} , the increase in ΔP and corresponding pumping power were prohibitively large. For example, the ΔP , mass flow rate and pumping power values for an HTC of 10⁶ W m⁻² K⁻¹ and a ΔT_{Max} of 27°C were 13000 kPa, 4.5 kg s⁻¹ and 60 kW, respectively. Therefore, while a high HTC is always desired, so that heat removal is efficient and independent of any change in HTC itself, it is not always economically viable to achieve it. Contrary to these high values, the selected case of 8 W pumping power yielded an HTC of 65 W m⁻² K⁻¹ with a

 ΔT_{Max} of 36°C. This constraint is much smaller than the total heat dissipated of 400 W by two pairs of IGBTs and diodes and therefore, is justified.

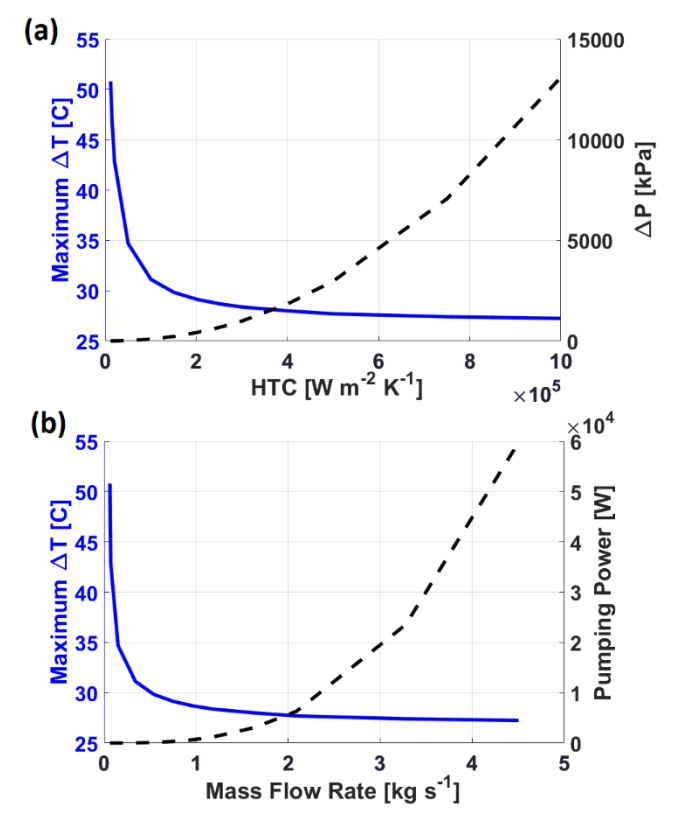


Figure 19. (a) Variation of ΔT_{Max} and ΔP with HTC for the best performing minichannel geometry – 2 mm square cross section (b) Variation of ΔT_{Max} and pumping power with HTC for the best performing minichannel geometry.

The computational analyses gave thorough insights into the fluid flow and heat transfer in these three geometries and better avenues to reduce ΔP and enhance HTC further can be explored based on these simulations. As the channel cooling was proved to be the best case, minor modifications in the channel designs, such as adding fillets at the channel entrance could further reduce the ΔP further by at least 20%. This could lead to increased coolant mass flow rate, in turn yielding an even better HTC value.

Finally, these channels were fabricated using reverse copper mold in the AlSiC heat sink to build a prototype package as shown in Figure 20. The channels have a 2 mm cross section and they run across the width of a single pair of devices. The set of channels is sealed with a cover plate that houses the inlet and outlet manifold to form a closed coolant loop. Such

prototypes have been subjected to fatigue and aging tests have shown excellent durability as discussed earlier.

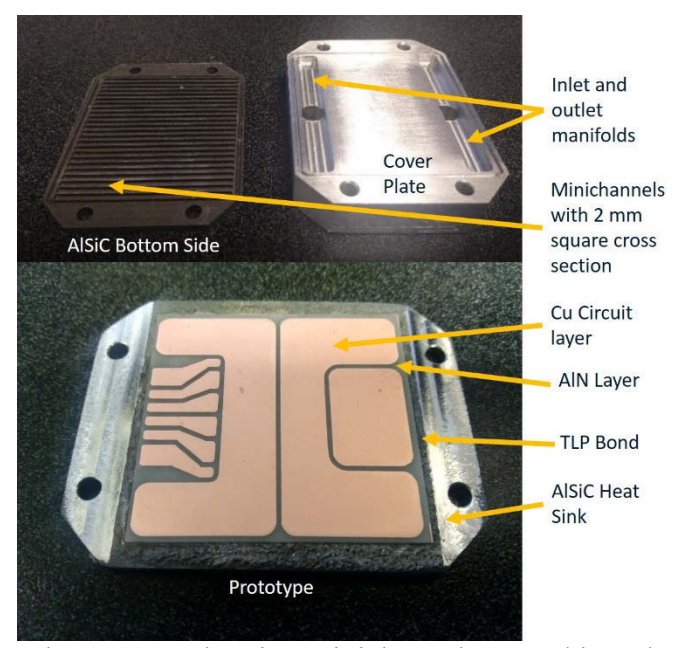


Figure 20. Fabricated prototype showing minichannels carved into the AlSiC heat sink.

5. CONCLUSION

An improved power electronics package that minimizes the interlayer CTE mismatch by directly bonding AlN to AlSiC heat sink is being investigated. The modified material layer sequence is Cu circuit layer – AlN dielectric – TLP bond – AlSiC heat sink, as compared to the conventional DBC (Cu – AlN – Cu) – solder – Cu base plate – thermal interface material – Al heat sink. This modification not only minimizes the CTE mismatch in the stack by up to 84%, thereby improving the lifetime of the package by at least 18 times under test conditions, but also makes the package more compact and light. This is because, a combination of 3 mm Cu base plate and 6 mm Al heat sink is replaced by a 3 mm AlSiC heat sink. The TLP bond has shown very promising mechanical, thermal and metallographic properties.

However, due to replacement of Cu layers with AlSiC, heat spreading and removal need to be upgraded to match the thermal performance of this package with that of DBC. Through thermal simulations, thin AlSiC plates with high HTCs were recommended, so that AlSiC-based

design remains thermally competitive with the conventional Cu-Al heat sinks. Next, channel flow, flow over pin fin and jet array cooling were investigated in this work and HTC and ΔP were optimized for each of the cooling scenarios for a fixed pumping power of 2% of the heat dissipated by an individual identical unit. While all single phase techniques competitive performance, minichannels were found to provide the best cooling performance with an HTC of 65 kW m⁻² K⁻¹ and a ΔP of 40 kPa. Heat spreading limitations of the AlSiC plate were overcome by the quick and efficient heat removal using channels. This resulted in a ΔT_{Max} of 36°C with channels, while that for the pin fin cooling and spray cooling were 38°C and 40°C for the same coolant pumping power. These temperature differences are minor, however, for a long term fatigue performance can induce a large difference, as to how many fatigue cycles the package can endure. It could be recalled that the ΔT_{Max} documented for a conventional package with the existing techniques was between 36°C and 39°C.

It must be noted this is a standalone comparison between channels, pin fins and jets for the power electronics geometry considered in the present work, when pumping power is kept constant for all three designs. While a comprehensive comparison is necessary that can transcend to any geometry, each of these designs have advantages in peculiar scenarios and their use can be appropriate in presence of specific requirements. For instance, a local hot spot can be effectively cooled by using localized jet cooling. This study provides insight into how much these three geometries can be effective in cooling the new AlN-AlSiC design being investigated by the authors [7].

6. ACKNOWLEDGEMENTS

The authors would like to thank the US Army Research Laboratory and the National Renewable Energy Laboratory for supporting this work.

7. DISCLAIMER

The views expressed in the article do not necessarily represent the views of the DOE or the U.S. Government. The U.S. Government retains and the publisher, by accepting the article for publication, acknowledges that the U.S. Government retains a nonexclusive, paid-up, irrevocable, worldwide license to publish or reproduce the published form of this work, or allow others to do so, for U.S. Government purposes.

8. REFERENCES

- [1] Blaabjerg, F., Zhe, C., and Kjaer, S. B., 2004, "Power electronics as efficient interface in dispersed power generation systems," IEEE Transactions on Power Electronics, 19(5), pp. 1184-1194.
- [2] Chen, Z., Guerrero, J. M., and Blaabjerg, F., 2009, "A Review of the State of the Art of Power Electronics for Wind Turbines," IEEE Transactions on Power Electronics, 24(8), pp. 1859-1875.
- [3] Emadi, A., Williamson, S. S., and Khaligh, A., 2006, "Power electronics intensive solutions for advanced electric, hybrid electric, and fuel cell vehicular power systems," IEEE Transactions on Power Electronics, 21(3), pp. 567-577.
- [4] Narumanchi, S., DeVoto, D., Mihalic, M., and Paret, P., 2013, "Performance and Reliability of Interface Materials for Automotive Power Electronics (Presentation)," National Renewable Energy Laboratory (NREL), Golden, CO.
- [5] Mitic, G., Beinert, R., Klofac, P., Schultz, H. J., and Lefranc, G., 1999, "Reliability of AlN substrates and their solder joints in IGBT power modules," Microelectronics Reliability, 39(6), pp. 1159-1164.
- [6] DeVoto, D., Paret, P., Narumanchi, S., and Mihalic, M., 2013, "Reliability of Bonded Interfaces for Automotive Power Electronics," (55751), p. V001T005A004.
- [7] Pahinkar Darshan, G., Puckett, W., Graham, S., Boteler, L., Ibitayo, D., Narumanchi, S., Paret, P., DeVoto, D., and Major, J., 2018, "Transient Liquid Phase Bonding of AlN to AlSiC for Durable Power Electronic Packages," Advanced Engineering Materials, 0(0), p. 1800039.
- [8] Wilson, J., 2007, "Thermal conductivity of common alloys in electronics packaging," M. Design, Compounds, Adhesives, Substrates, ed.
- [9] Wei, R., Song, S., Yang, K., Cui, Y., Peng, Y., Chen, X., Hu, X., and Xu, X., 2013, "Thermal conductivity of 4H-SiC single crystals," Journal of Applied Physics, 113(5), p. 053503.
- [10] Incropera, F. P., DeWitt, D. P., Bergman, T. L., and Lavine, A. S., 2007, Fundamentals of Heat and Mass Transfer, John Wiley and Sons.

- [11] Siewert, T., Liu, S., Smith, D. R., and Madeni, J. C., 2002, "Database for Solder Properties with Emphasis on New Lead-free Solders," Properties of Lead-Free Solders Release 4.0 N. I. o. S. a. T. C. S. o. Mines, ed.Colorado.
- [12] Zhou, F., Dede, E. M., and Joshi, S. N., "A novel design of hybrid slot jet and mini-channel cold plate for electronics cooling," Proc. 2015 31st Thermal Measurement, Modeling & Management Symposium (SEMI-THERM), pp. 60-67.
- [13] Lau, B. L., Han, Y., Yue, G., Lu, Z., and Xiaowu, Z., "Fabrication of package level silicon micro-cooler for electronics cooling," Proc. 2015 IEEE 17th Electronics Packaging and Technology Conference (EPTC), pp. 1-7.
- [14] Sakanova, A., and Yin, S., "Comparative investigation of double-layer and double-side micro-channel cooling for power electronics packaging," Proc. 2013 IEEE 15th Electronics Packaging Technology Conference (EPTC 2013), pp. 73-77.
- [15] Pautsch, A. G., Gowda, A., Stevanovic, L., and Beaupre, R., 2009, "Double-Sided Microchannel Cooling of a Power Electronics Module Using Power Overlay," (43604), pp. 427-436.
- [16] Maddox, J. F., Knight, R. W., and Bhavnani, S. H., "Local thermal measurements of a confined array of impinging liquid jets for power electronics cooling," Proc. 2015 31st Thermal Measurement, Modeling & Management Symposium (SEMI-THERM), pp. 228-234.
- [17] Gess, J. L., Bhavnani, S. H., and Johnson, R. W., 2015, "Experimental Investigation of a Direct Liquid Immersion Cooled Prototype for High Performance Electronic Systems," IEEE Transactions on Components, Packaging and Manufacturing Technology, 5(10), pp. 1451-1464.
- [18] Turgut, A., and Elbasan, E., "Nanofluids for electronics cooling," Proc. 2014 IEEE 20th International Symposium for Design and Technology in Electronic Packaging (SIITME), pp. 35-37.
- [19] Malu, N., Bora, D., Nakanekar, S., and Tonapi, S., "Thermal management of an IGBT module using two-phase cooling," Proc. Fourteenth Intersociety Conference on Thermal and Thermomechanical Phenomena in Electronic Systems (ITherm), pp. 1079-1085.
- [20] CERN, 2011, "Properties of mixture Water/Glycol," http://detector-cooling.web.cern.ch/Detector-Cooling/data/Table%208-3-1.htm.
- [21] Churchill, S. W., 1977, "Comprehensive Correlating Equations for Heat, Mass and Momentum Transfer in Fully Developed Flow in Smooth Tubes," Ind. Eng. Chem. Fund., 16, pp. 109-116.
- [22] Churchill, S. W., 1977, "Friction-Factor Equations Spans All Fluid Flow Regimes," Chem. Eng.-New York, 84, p. 91.
- [23] Munson, B. R., Young, D. F., and Okiishi, T. H., 2006, Fundamentals of fluid mechanics, Hoboken, NJ: J. Wiley & Sons.
- [24] Zukauskas, A., and Ulinskas, R., 1988, Heat Transfer In Banks Of Tubes In Crossflow, Hemisphere Publishing Corporation.